Influence of the nanostructure on the electric transport properties of resistive switching cluster-assembled gold films

Francesca Borghi[1], Matteo Mirigliano[1], Davide Dellasega[2], Paolo Milani[1]*

1 CIMaINa and Department of Physics, Università degli Studi di Milano,

via Celoria 16, 20133 Milano, Italy

2 Department of Energy, Politecnico di Milano, via Ponzio 34/3, 20133 Milano, Italy

Abstract

The use of Au clusters produced in the gas phase and deposited at low kinetic energy on a substrate allows the bottom-up fabrication of nanostructured metallic thin films with an extremely large number of interfaces, grain boundary junctions and crystal lattice defects. Cluster-assembled gold films exhibit non-ohmic electrical transport properties with a complex resistive switching behavior, exploring discrete resistance states which depend on their structural features (average thickness, resistance value reached on the percolation curve). Their electric conduction properties can be modelled in terms of complex networks of nanojunctions and used to perform binary classification of Boolean functions. The fabrication of devices based on cluster-assembled Au films and exploiting emergent complexity and collective phenomena requires a deep understanding of the influence of the nanoscale structure on the fundamental mechanisms of electrical conduction. Here we present a detailed study of the correlation between the nanostructure and the electrical properties of cluster-assembled gold films by a systematic characterization of the film growth from sub-monolayer to continuous layer beyond the electrical percolation threshold. The influence of different cluster size distributions on the onset of the electrical conduction and the role of defects is investigated by combining in situ and ex situ electrical and structural characterizations.

Keywords: gold clusters, nanostructured thin films, electrical properties, percolation, memory effect.

Introduction

The electrical conduction properties of polycrystalline thin metal films are described by Ohm laws and their resistivity increases with the decreasing of film thickness due to the scattering effects of conduction electrons at surfaces and defects [1–3]. The improvement of the electric transport properties of ultrathin metallic structures is actively pursued aiming at the reduction of the defect density in order to meet the requirements of extremely high integration of devices and hence the drastic downscaling of the interconnect dimensions [1,2,4].

However, the large number of defects and grain boundaries in metallic thin films is not always to be considered as detrimental: systems made by nanoscale components are characterized by a drastic increase in the volume fraction (and importance) of grain boundaries and grain-grain junctions, in particular those based on grains with dimensions below 100 nm, are expected to show novel structural and functional properties compared to their classical counterpart fabricated by assembling atoms or molecules [5–7]. Metallic thin films, near the percolation threshold, have been reported to show interesting resistive switching phenomena [8,9].

The use of metallic clusters or nanoparticles produced in the gas phase and deposited on a substrate, has emerged recently as an interesting approach for the bottom-up fabrication of nanostructured metallic thin films: upon deposition at low kinetic energies, metal clusters retain their individuality producing a nanogranular layer with an extremely large number of interfaces, grain boundary junctions and crystal lattice defects [5,6]. At odd with their polycrystalline counterparts, cluster-assembled metallic films exhibit non-ohmic electrical transport properties with a complex resistive switching behaviour [5,10,11]. We remark that this behaviour survives also for higher thickness, beyond the percolation threshold. In particular Au cluster-assembled thin films recurrently and discretely explore resistance states which depend on their structural features (average thickness, resistance value reached on the percolation curve) [11], in contrast to what happens in gold thin film near percolation threshold, where an on-off behaviour is observed [8,9]. the non-linear electric behaviour is remarkably stable and reproducible allowing the exploration of well-defined resistive states [11]. Their electric conduction properties can be modelled in terms of complex networks of nanojunctions [12].

Recently we demonstrated that Au cluster-assembled films can be used to fabricate a device, called receptron, performing binary classification of Boolean functions [13]. This can open interesting perspectives in the field of unconventional computing (UCOMP) based on the use of hardware and physical architectures relying on emergent complexity and collective phenomena originating from various classes of physical substrates [14]. In order to assess reliable bottom-up fabrication

approaches based on nanoparticle assembling, a deep understanding of the influence of the nanoscale structure on the fundamental mechanisms of electrical conduction is necessary.

Here we present a detailed study of the correlation between the nanostructure, in terms of primeval cluster size and growth mode of the film, and the electrical properties of cluster-assembled gold films by a systematic characterization of the film growth from sub-monolayer to continuous layer beyond the electrical percolation threshold. The influence of different cluster size distributions, which enhance the role of defects and grain boundaries on the onset of the electrical conduction is investigated by combining in situ and ex situ electrical and structural characterizations.

2. Materials and methods

2.1 Cluster-assembled film deposition

Nanostructured gold films are produced by a supersonic cluster beam deposition (SCBD) apparatus equipped with a pulsed microplasma cluster source (PMCS), as described in detail in [5,15,16] (Fig. 1).

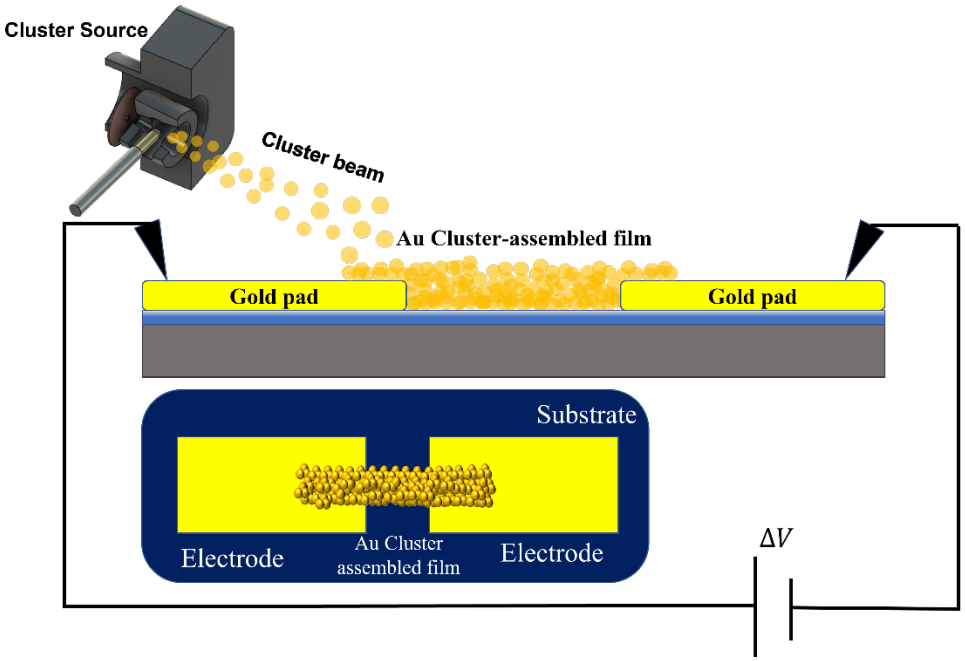

Figure 1. Schematic view of cluster source (top-left) combined with a cross-section and a top-view of the ns-Au device: two pre-evaporated gold electrodes are bridged by a ns-Au film. The cluster beam is focused on the substrate, while a two-probe resistance measurement is performed during the deposition.

The SCBD set-up schematically consists of three differential pumped vacuum chambers. The first chamber hosts a PMCS where the injection of an inert gas, the production of clusters in gaseous phase is realized through the ablation of a metal target by a discharge plasma. The cluster-gas mixture is

then extracted to form a supersonic seeded beam that impinges on a substrate fixed on a sample holder perpendicular to the beam trajectory [5]. The quantity of mass deposited (expressed in microbalance equivalent thickness) is monitored by a quartz microbalance integrated in the sample holder. We used different carrier gases (He and Ar), in order to produce different cluster mass distributions: in particular clusters produced with He have a lower mass distribution than that those produced by using Ar [17]. In order to change the mean size of the particles with the same gas carrier, it is possible to tune the time interval between gas injection and ignition of the discharge. Cluster-assembled films produced by He and Ar as carrier gases are called ns-Au/He and ns-Au/Ar respectively.

Cluster-assembled films have been deposited on oxidized silicon substrates with two gold evaporated electrodes (2mm x 7 mm) separated by 1 mm gap (Fig. 1). Silicon substrates were cleaned using an ultrasonic bath and subsequently heated in air at 900°C for 4 hours in order to induce the formation of an oxide homogenous insulating layer with a surface roughness of 0.34 nm, measured by atomic force microscopy (AFM). Standard polycrystalline gold thin films have been deposited by thermal evaporation of gold in high vacuum (10^{-6} torr) using an Edwards E306A coating apparatus with a deposition rate of 0.01 - 0.005 nm/sec.

The in situ characterization of the electrical behavior of gold thin films correlated to the quantity of mass deposited (i.e. percolation curves) has been performed with a multimeter (Agilent model 34410A), controlled by a homemade LabView routine, that allows data acquisition through electrical contacts connected to the sample in the deposition chambers.

2.2 Morphology characterization

Topographical maps of the nanostructured gold films have been acquired in air using a Multimode AFM equipped with a Nanoscope IV controller (BRUKER). Rigid silicon Tapping Mode cantilevers mounting single crystal silicon tip with nominal radius 5–10 nm and resonance frequency in the range 250–350 kHz have been used. Several 2 μm × 1 μm images were acquired on each sample with scan rate of 1 Hz and 2048 × 512 points. The images were flattened by line-by-line subtraction of first and second order polynomials in order to remove artifacts due to sample tilt and scanner bow, and subsequently analyzed in Matlab environment.

The height of the primeval incident gold clusters was measured by AFM images of the sample with very low surface coverage; in particular its value was identified by the peak of the log-normal distribution of the clusters height by several images acquired on the same sample. More details are reported in [18]. Root-mean-square surface roughness (Rq) was calculated from AFM images as the standard deviation of surface heights.

The evolution of film growth (maximum island area and coverage) was performed through the analysis of images acquired by a Scanning Electron Microscope (Zeiss Supra 40). Several grayscale images have been acquired with a 5 kV electron beam at different magnifications (300–1000 kX), with a resolution of 1.2 nm/ pixel. The grayscale imaging process, which consists in the binarization of the images and the analysis of the geometrical properties of the identified objects, is extensively described in [18,19].

Gas adsorption measurements for the evaluation of the film porosity were performed employing a Gemini surface area analyzer (Micromeritics, model 2365), according to the method reported in [20]. Before each measurement, samples were degassed under a constant helium flux at 110 °C for 2 h using a dedicated unit, in order to remove any contaminants which may affect the measurements. The degassing temperature was carefully selected in order to be non-invasive for gold structure; this statement was verified by AFM measurements of surface morphology before and after annealing treatment. The specific surface area (A_{BET}, expressed in m^2/g) was calculated considering the relative pressure interval between 0.05 and 0.25.

Film density is determined by AFM characterization of film thickness in order to provide a correction factor to the microbalance measurements acquired in-situ: the ratio between the AFM and the microbalance density is the reciprocal of the ratio between the corresponding thicknesses.

3. Results and Discussion

3.1 Morphological evolution of nanostructured gold films with coverage

Figure 2 shows the AFM morphological maps of the ns-Au/Ar film for three different stages of growth, from the bare oxidized silicon substrate (a) to a 110 nm thick film (d).

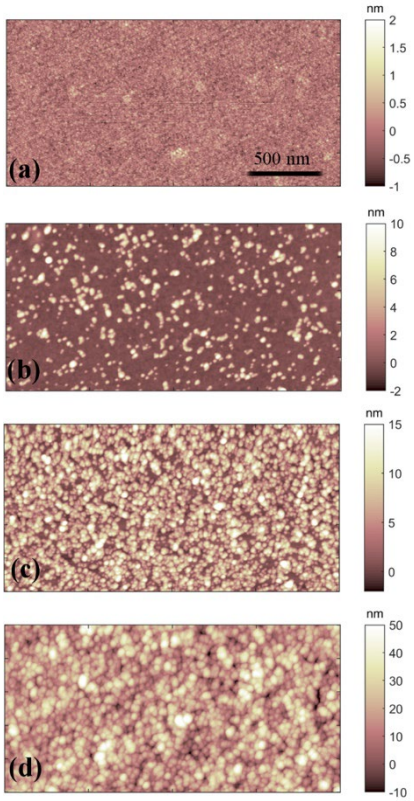

Figure 2. (a) AFM morphological maps of oxidized silicon substrate and (b-d) ns-Au/Ar films with increasing quantity of gold clusters deposited (corresponding to 3 nm, 20 nm and 110 nm microbalance thickness).

The height distributions of the primeval incident gold clusters deposited on the substrate have been obtained by AFM characterization of ns-Au films at very low coverage: Figure 3 shows the distributions of the heights of the objects identified by AFM imaging, with substrate coverage of 8% for ns-Au/He and of 11% for ns-Au/Ar films, in semi-log scale. The lateral dimension of the objects identified on the AFM map is not of reference actually due to the effects of the convolution with AFM tip [18], while the estimation of the height is accurate within the fraction of nanometer.

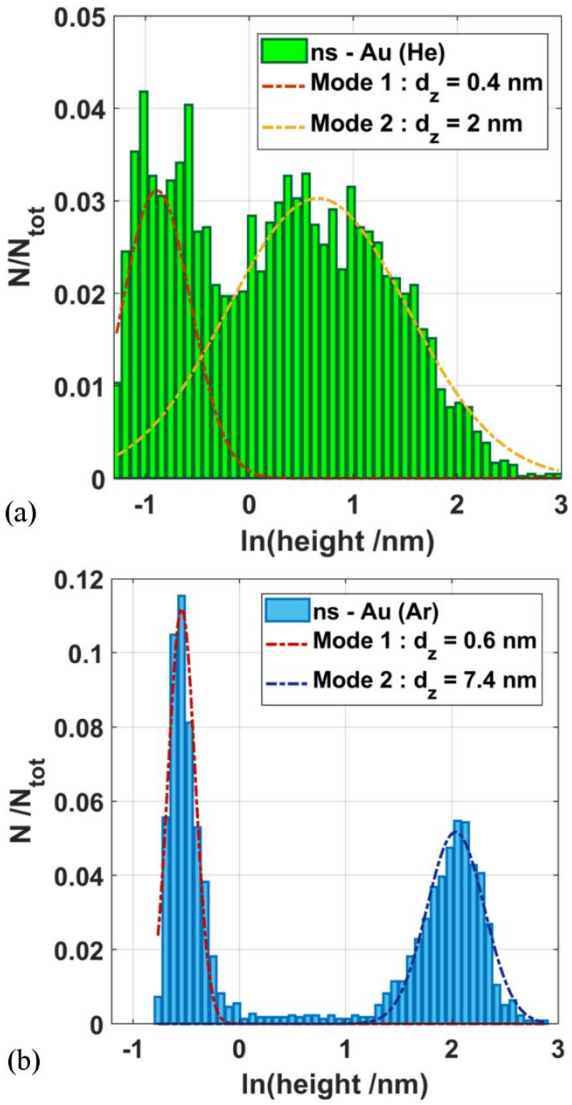

Figure 3. Distribution of the height of ns-Au/He (a) and ns-Au/Ar (b) primeval incident clusters in semi-log scale, calculated by AFM topographical maps with 8% and 11% coverage.

We observe, for both systems, a bimodal log-normal distribution in analogy to what has been reported for zirconia and titania clusters deposited by SCBD [18,20,21]. The first mode of the distributions, centered in 0.4 and 0.6 nm for ns-Au/He and ns-Au/Ar respectively, is representative of the smallest gold clusters with a short residence time in the PMCS [16]. Their mobility on the substrate is higher compared to that of the larger clusters (second peak of the distributions), while their contribution in the mass changes registered by microbalance is very low. The ratio between the areas subtending the two peaks of the distribution is 0.4 and 1 for ns-Au/He and ns/Ar samples respectively. The second mode of the distributions is centered in 2 and 7.4 nm for ns-Au/He and ns-Au/Ar respectively; this peak characterizes the two different systems and it will be considered as the cluster typical dimension hereafter.

The evolution of the morphology of cluster-assembled structures on the oxidized silicon surface with coverage (defined as the ratio of the area occupied by particles and the overall area) could be in principle described by different models used for atom-assembled thin films [22], although many elementary processes, such as clusters diffusion, are slower compared to atomic systems [23]. A model based on the three main physical mechanisms of a cluster-assembled film growth is the deposition, diffusion, and aggregation (DDA) model [23], which we refer to. The understanding of the mechanism governing the thin-film growth and the description of its morphological properties allows to better appreciate the connectivity of cluster and to interpret the electrical conduction properties.

In order to visualize and compare the different gold thin film morphologies and their evolution with coverage, Figure 4a-c reports scanning electron microscopy (SEM) images of evaporated atom-assembled gold, ns-Au/He and ns-Au/Ar films, according to an increasing surface coverage ranging from 8 to 40 %.

The evolution of the maximum area size (identified as the peak with highest abscissa in the area distribution of the objects in the AFM images) with coverage (Figure 4d) suggests that in ns-Au/He systems gold islands grow very rapidly, compared to ns-Au/Ar and to the atom-assembled film, while the substrate where polycrystalline gold films are grown by evaporation has the largest number of objects identified on the surface (Fig. 4e). Both ns-Au/He and evaporated gold films grow in a 2D mode: the former by enlarging the pre-existing islands, the latter by occupying all the defects of the substrate with new small islands. This hypothesis is confirmed also by the evolution of roughness with coverage (Figure 4f) which is associated to the film growth in z-direction: roughness of ns-Au/He samples shows a flat evolution while the evaporated systems provide a decreasing trend, from the pristine oxidized silicon roughness value (0.34 nm, purple cross marker in Figure 4f) to 0.2 nm. The shape of the evaporated gold and ns-Au/He islands is also relevant: the process of island growth can be considered as related to characteristic times. If the time interval before a new cluster is deposited on another is longer than coalescence time, the island can reach a compact spheroid shape before another cluster arrives. In the opposite case, the island does not have time to change into a compact shape before the arrival of the next cluster and hence it evolves into a non-compact and ramified shape [24]. The fractal dimension of islands formed on the surface provides an important information concerning their shape. From the analysis based on the evolution of the islands area versus their perimeters we calculated fractal dimension; it does not evolve with coverage and corresponds to 1.22 ± 0.02, 1.46 ± 0.03 and 1.29 ± 0.03 for evaporated atom-assembled gold, ns-Au/He and ns-Au/Ar films accordingly. The samples composed by ns-Au/He clusters are characterized by highest fractal dimension, since clusters are small enough to diffuse on the oxidized

silicon surface, as confirmed by the 2D growth evidences discussed before, but they are too big to coalesce in a compact rounded shape differently from gold evaporated films.

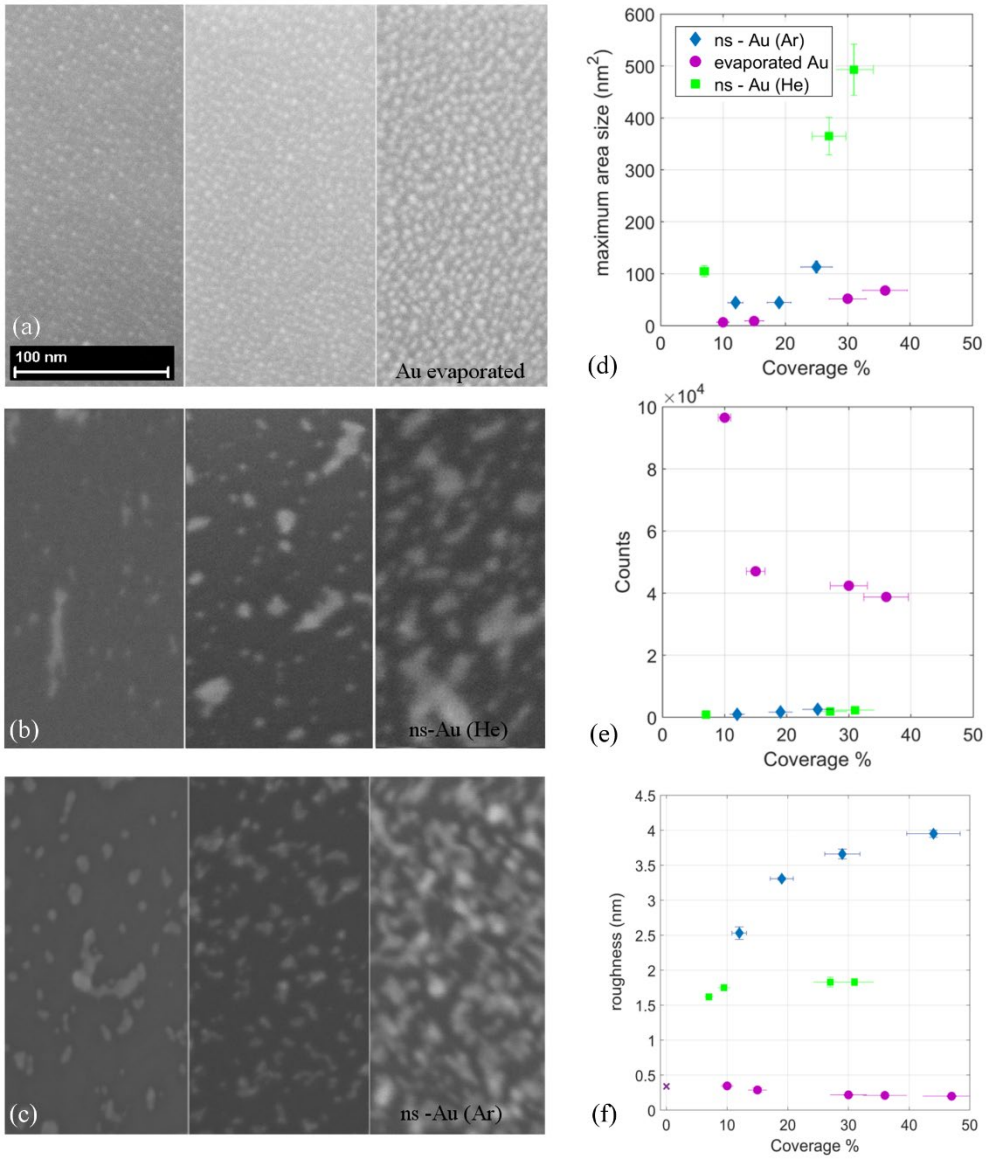

Figure 4. SEM micrographs of systems with increasing surface coverage (from 8 to 30% approximately) (a) evaporated (atom-assembled) gold, (b) ns-Au/He, (c) ns-Au/Ar samples. Maximum area size (d), counts of objects (e) and RMS roughness (f) as a function of surface coverage are obtained by a quantitative analysis of the SEM images.

Ns-Au/Ar films show a moderate growth of the maximum surface area (figure 4d), a slow increase (as ns-Au/He) of the number of islands (figure 4e), and a fast increase of the surface roughness (figure 4f), according to a 3D growth. At odd with the evaporated atoms and the ns-Au/He clusters, which can diffuse with highest probability on the substrate, the 7 nm large ns-Au/Ar clusters stick to the oxidized silicon substrate and their diffusion is negligible.

The dependence of surface coverage with deposition time reveals also the mechanism of particle-particle diffusion. According to DDA model [25,27], assuming that all the primeval incident clusters contribute to the increase of surface coverage, i.e. incoming clusters can diffuse on the top of those already deposited and reach the substrate, the increase of surface roughness with deposition time is expected to be linear [25–27]. Otherwise, if the incoming particles are blocked and prevented from touching the substrate, the evolution of surface coverage with time is described by an exponential law [18,25]. Since both atoms and clusters deposition rate is stable in time, the evolution of coverage can be studied as a function of deposited thickness. Figure 5 shows the evolutions of surface coverage with microbalance thickness for evaporated gold, ns-Au/He and ns-Au/Ar films.

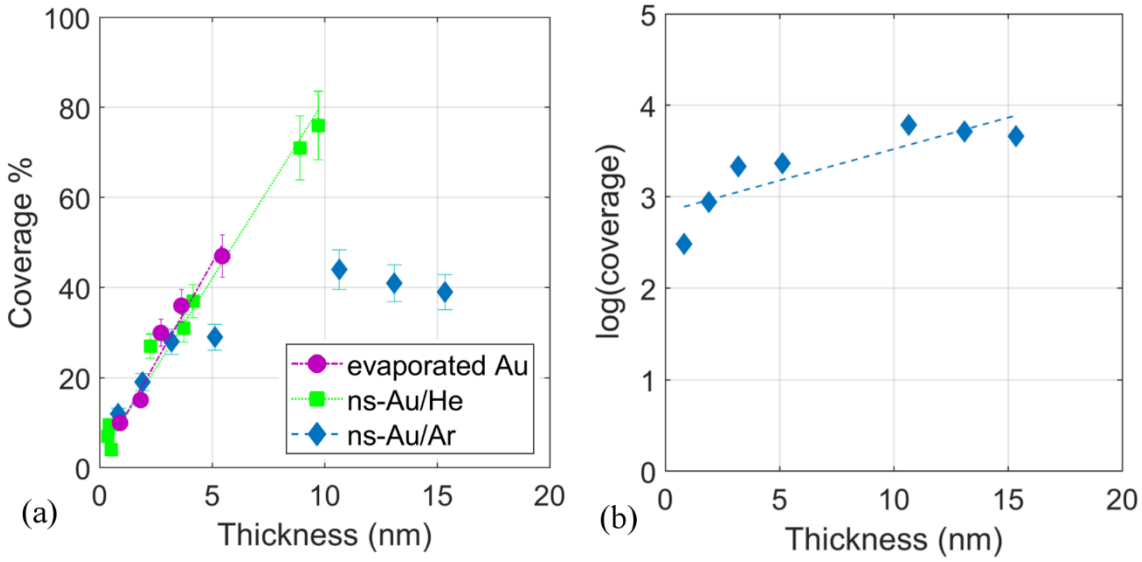

Figure 5. (a) Surface coverage as a function of microbalance thickness; (b) evolution of surface coverage for ns-Au/Ar samples in semilog scale.

The linear increase of coverage with thickness for evaporated gold and ns-Au/He samples confirms our hypothesis concerning the 2D growth mode for these systems [25–27]. On the other hand, the linear trend in semi-log scale of ns-Au/Ar surface coverage with thickness (shown in Figure 5.b) is an evidence of the different growth mode for this system, constituted by larger clusters, and which is compatible with a 3D growth model [25–27].

3.2 Morphological growth beyond the geometrical percolation

Surface roughness evolves with thickness according to a power law [28] $Rq \sim t^{\beta}$, for all the three systems analysed. As it is graphically shown in Figure 6, the growth exponent of ns-Au/He and

ns-Au/Ar films is the same, and it corresponds to $\beta \sim 0.4$. The roughness of evaporated gold films increases more slowly with $\beta \sim 0.33$.

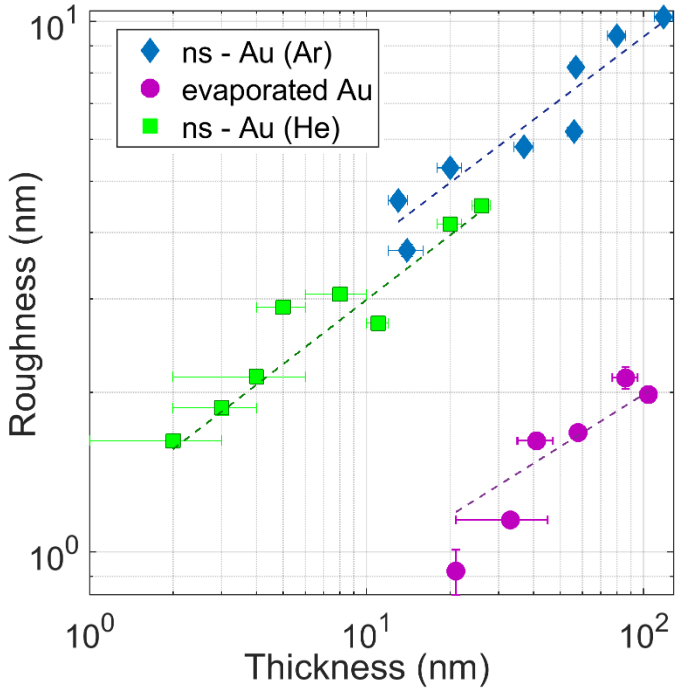

Figure 6. Roughness of evaporated and cluster-assembled gold thin films versus thickness in log-log scale.

The identical growth exponent for films grown with different cluster size distributions suggests a similar growth mode after the first layers are formed. In particular, $\beta \sim 0.4$ correspond to the growth exponent of a ballistic deposition model [29], where incoming particles stick upon landing without significantly diffusion around the first contact with the pre-deposited clusters, according to a sticking probability correlated principally to the incident cluster size [30,31]. This growth characterizes cluster-assembled thin film of many materials deposited by SCBD [18,32,33].

The resulting cluster-assembled films are characterized by a nanoscale granularity and high porosity: in Table 1 the structural properties of the gold thin film deposited on oxidized silicon substrate characterized by gas adsorption measurements are shown.

sample	density (g/cm^3)	porosity	A_{BET} (m^2/g)
Evaporated gold	17.29	0.1	170
ns-Au/He	9.54	0.5	630
ns-Au/Ar	8.56	0.6	260

Table 1. Structural properties of gold thin films derived from gas adsorption measurements.

In spite of the expected weak porosity of the evaporated gold film, its specific surface area is not negligible. This result is due to the particles size of the thin films: by decreasing their dimensions, the surface/volume ratio increases while the contribution of the overall porosity remains low. For the same reason, specific surface area of ns-Au/He is higher than for ns-Au/Ar films.

3.3 Evolution of the electrical properties with film topology

The in situ electrical characterization allows to directly correlate the information concerning the quantity of mass deposited and the evolution of the electrical resistance for increasing film thickness. By recording the resistance as a function of thickness we obtained the percolation curve.

The trend of the percolation curve for nanogranular metallic films is determined by several parameters like deposition rate [34], particle size [35] and crystallization processes that can occur during the growth [36]. It was also inferred that the percolation process can be influenced by the presence of electrical contact with a broad distribution of conductivity among the deposited clusters [27]. However, the correlation between electrical conduction properties and structural properties granular films is still far from being completely understood [5].

Percolation curves acquired from evaporated gold, ns-Au/He and ns-Au/Ar thin films (Figure 7a) show that the drastic fall of resistivity happens according to particles dimension: first evaporated gold, in agreement with values reported in literature [37], followed by ns-Au/He and finally by ns-Au/Ar films. Small particles are more effective in forming large, well-connected regions during the film growth [27], reaching a fully percolated film at low thickness values.

In Figure 7b we plot conductance of the same curves shown in Figure 7a, in order to highlight the behavior for higher thickness values. We focus on conductance instead of conductivity in order to avoid the contribution of the thickness error in the curves and to provide the best description of the conductance evolution during the deposition. By plotting the film conductances (figure 7b), we observe that evaporated gold films show the faster increase in the conductance beyond the percolation threshold, while ns-Au/He films show lower conductance values with respect to ns-Au/Ar for the same thickness values. This result suggests that particle dimension is not the only parameter that influences the percolation process and the evolution of electrical conductivity during the growth of granular films.

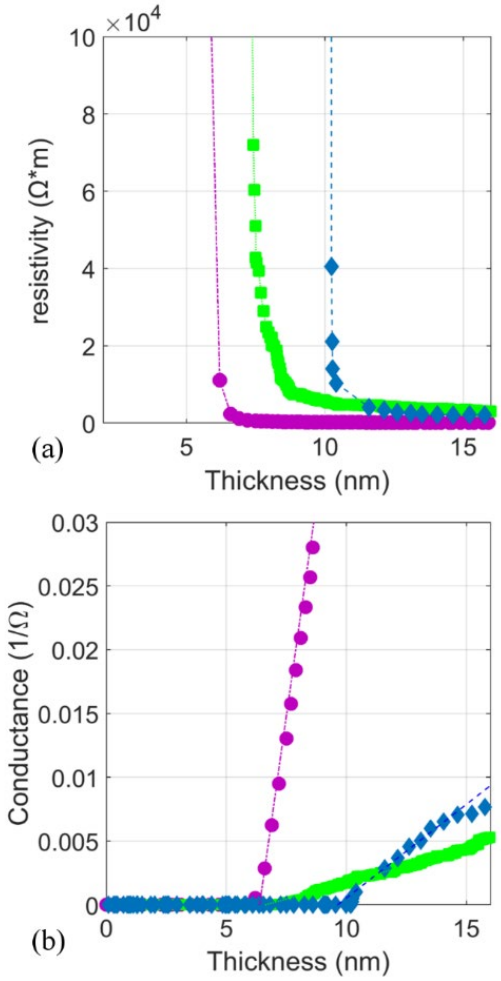

Figure 7. Resistivity (a) and conductance (b) of evaporated gold, ns-Au/He and ns-Au/Ar samples.

The slope of the linear increase of conductance versus thickness is ∼ 0.013 for the evaporated films, while it is one order of magnitude lower for ns-Au/Ar (∼ 0.0015) and even more for ns-Au/He (∼ 0.0005). Cluster-assembled systems show a substantial difference from atom-assembled thin films, since their conductivity increases at a slower rate with a slope dependent from the cluster dimensions. In Figure 7b a pronounced gap appears between the maximum conductance reached for atom-assembled films compared to the cluster-assembled ones, highlighting a fundamental difference between the two systems due to their different nanoscale granularity. The results could be explained considering that cluster do not lose their structure during the film growth process : this determines the presence of a very high density of grain boundaries and defects that limits the electron conduction capability in cluster-assembled films compared to the atom-assembled ones [5]. In atom-assembled films, grains grow during the atom deposition thanks to diffusion and aggregation process resulting in polycrystalline structure [38].

The comparison between percolation curves obtained from systems fabricated with different particle mass distributions should be conducted by considering that different microbalance

thicknesses may correspond to identical surface coverage. Starting from this observation, we rescaled the percolation curves shown in Figure 7 as a function of surface coverage according to the experimental coverage-thickness curve reported in Figure 5a; the results are plotted in Figure 8.a.

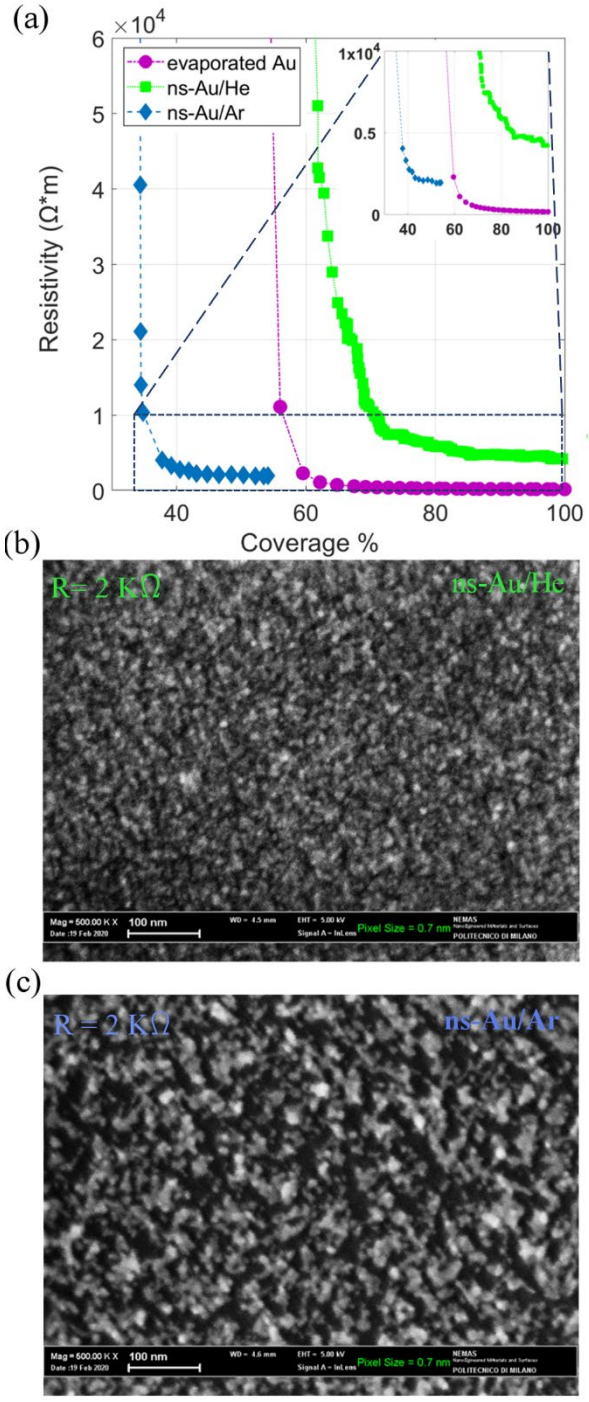

Figure 8. (a) Resistivity of evaporated gold (violet line), ns-Au/He (green line) and ns-Au/Ar (blue line) as a function of coverage, in the inset the enlarged region characterized by low resistivity is shown; SEM images of ns-Au/He (b) and ns-Au/Ar (c) samples characterized by the same value of resistance (R ∼ 2 KΩ).

The resistivity of the three systems as a function of coverage shows the lower percolation threshold for ns-Au/Ar, at odd with what is reported in Figure 7 where the conductance is plotted

against the film thickness. In addition, ns-Au/He and ns-Au/Ar percolation curves invert their relative position in the graph with respect to Figure 7.

The coverage percolation threshold ξ_C should depend only on the dimensionality of the system [39] ($\xi_C \sim 0.16$ in 3D, $\xi_C \sim 0.45$ in 2D). In the case of atom-assembled films, the threshold value is close to the predicted value and in agreement with what is reported in literature [37]. This confirms that atomic-deposition favors the formation of 2D islands on the surface, forming large and connected structures. On the other hand, the curves obtained from cluster-assembled films demonstrate a departure from the standard percolation theory. In fact, phenomena like coalescence and overlapping of grains with different size, internal structure and different electrical properties can cause an evolution different from that predicted by the percolation theory. In particular, the low percolation threshold for ns-Au/Ar suggests the influence of a 3D growth in film with higher dimensions. Moreover, SEM micrographs of ns-Au/He and ns-Au/Ar thin films with the same resistance value (R $\sim$ 2 KΩ) (Figure 8 b and c), confirm that different coverages such as 39 % ± 2 % for ns-Au/Ar and 72 % ± 3 % for ns-Au/He samples can have the same electrical resistance.

The behavior of the percolation curve of ns-Au/He (green curve in Figure 8a) deserves a particular attention: the percolation threshold the resistivity substantially different from both the atom-assembled and the ns-Au/Ar films cannot be explained only by considering the coalescence and diffusion phenomena occurring during the growth. One has to consider also the density of grain boundaries and defects generated during the cluster assembling and its influence on the electrical conduction [1,2]. The small grain size of ns-Au/He films causes a higher density of grain boundaries with respect to ns-Au/Ar films, strongly influencing the electron motion and contributing to the appearance of the anomalous trends in the percolation curve by affecting the conduction electron mean free path and the free electron density [1,2].

3.4 Conductivity in cluster-assembled thin films beyond electrical percolation

In order to deeply understand the influence of the granular structure at the nanoscale on the electron transport properties we analyzed the percolation curves, using Namba model, as described in [40]. The expression of the conductivity [41] is

$$\sigma(\bar{t}) = \sigma_\infty \frac{L}{\bar{t}} \left[\int_0^L \frac{\sigma_\infty}{\sigma\{t(x)\} t(x)} \right]^{-1} \quad (1)$$

where L is the length of the film in the current flow direction, σ_∞ is the conductivity of a film of infinite thickness [42], $t(x)$ is the thickness of the film that takes into account the surface roughness and it is approximated by the expression $t(x) = \bar{t} + h\sin(2\pi x/s)$ (where h is the roughness and s the

correlation length as defined in [33]). $\sigma\{t(x)\}$ is the value of the local conductivity of a film with thickness t. Here we analyze the evolution of the conductivity as a function of thickness in the framework of Fuchs model [42], where it is assumed that electrons flowing through a thin metallic film can undergo elastic or inelastic scattering near the surfaces. Hence, an approximation of $\sigma\{t(x)\}$ is given by Sondheimer formula [42]:

$$\frac{\rho(t)}{\rho_\infty} = 1 + \frac{3}{8}\frac{l}{t}(1-p). \qquad (2)$$

In equation 2 l is the mean free path of an infinite thick film and p is a coefficient that takes into account the fraction of elastically scattered electrons from the surfaces, while $1-p$ is the fraction of randomly scattered electrons [42]. We underline the fact that the present model does not take into account the grain boundary contribution to electrical resistivity, standard semiclassical models including electron-grain boundary scattering can be found in [43,44]. These models have been developed for polycrystalline thin films where the dimensions, density and evolution of grain boundaries with thickness are substantially different from the case of nanogranular cluster-assembled films [5,6]. For this reason, we decided to consider a less sophisticated model with the aim to describe at least some basic features of a very complex system.

We insert the modified expression of resistivity, given by Drude formula [40], $\rho_\infty = \left(\frac{e^2 n_0 l}{m v_F}\right)^{-1}$ in Namba equation, where e is the electron charge, l the mean free path, m the electron mass, v_F the Fermi velocity and n_0 is an effective electron density. The last parameter takes into account the real fraction of conduction electrons that contribute to the current flowing, which is reduced with respect to the one of a bulk metal [45]. The fitting procedure described in Ref. [40] allows us to obtain information about the electron mean free path and the effective electron density. The other terms in the expression of Drude formula (e, m, v_F) are fixed parameters, and we have chosen the ones used in literature for gold polycrystalline films [46].

We used equation (2) to fit the curve ρt vs. t, where ρ is the resistivity and t is average thickness of the cluster-assembled film. The resistivity is computed as the product of the sheet resistance multiplied by the average film thickness. In order to choose the fitting boundaries, we considered the lower one as the minimum in ρt vs. t curve (t_{min}), while the maximum one is the thickness value reached at the end of the deposition. From the modified Drude formula, the mean free path l, the effective free electron density n_0, and parameter p can be extracted.

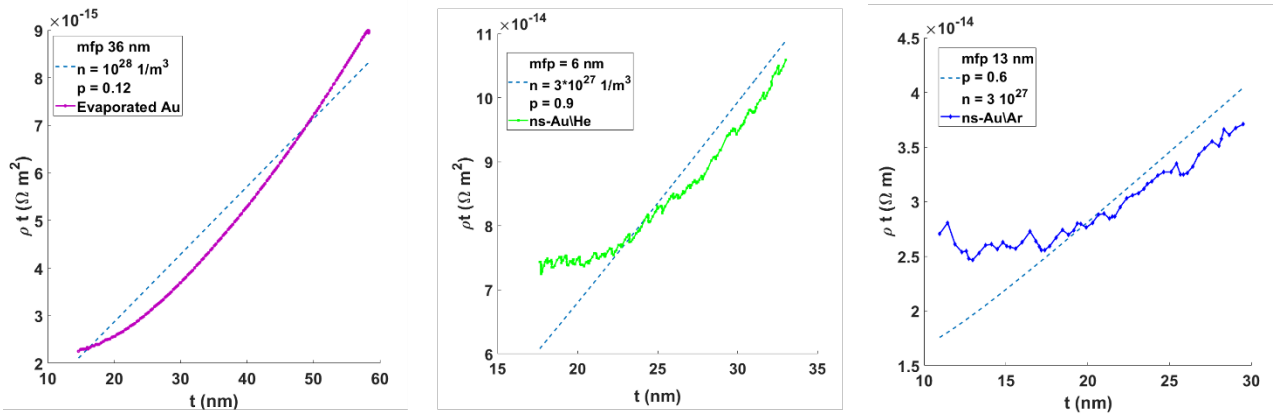

Figure 9. Percolation curves fitted through the Namba's model expression for (a) evaporated gold, (b) for ns-Au/He and for (c) ns-Au/Ar films.

Figure 9 shows the experimental curves ρt vs. t for an atom-assembled film (panel a) and cluster-assembled films, ns-Au/He and ns-Au/Ar respectively (panel b and c). The graphs in Figure 10 are plotted for values of thickness larger than t_{min}, the thickness threshold above which the films are continuous and fully connected.

The results obtained for the atom-assembled films are used as reference in order to compare the results obtained for cluster-assembled films. The atom-assembled films show mean free path in the range 24 nm - 33 nm and an effective electron density of the same order of magnitude of the bulk one [3]. The parameter p results always in a value lower than 0.5.

For cluster-assembled films we observe (Figure 9.b-c) that the curves are well fitted only for high thicknesses (above 15 nm); at low thickness, the fitted curve diverge and non-linear conduction mechanisms take place. Electron mean free paths in ns-Au films are considerably smaller than that of bulk and atom-assembled films. The smallest values result for the ns-Au/He samples, with mean free path lower than 9 nm, while ns-Au/Ar films have a mean free path in the range from 13 nm to 20 nm.

Parameter p results above the value 0.5 for ns-Au/Ar films. This suggests that the percolation curve is well described by equation (2) if a fraction of electrons is considered randomly scattered at the surfaces. Highest values appear for ns-Au/He sample class, where the parameter p is higher than 0.8. The density of free electron for ns-Au/He and ns-Au/Ar samples is one order of magnitude smaller than that of bulk gold [3].

Our results suggest that the models used to describe the electron conduction in polycrystalline metallic thin films only partially capture the mechanisms that regulate the electron transport in cluster-assembled systems. Pure geometrical considerations can explain only some differences in the percolation curves of atom-assembled and cluster-assembled films: the different dimensions of the

building blocks in the two cases affect the formation of a continuous layer with the consequence of having different resistances for the same thickness values. The different grain sizes and densities present in atom-assembled, ns-Au/He and ns-Au/Ar films, are due to different diffusion coefficients: for atom-assembled films the grain size grows with the thickness and the grain density lowers accordingly [38], whereas the dimensions of grains in cluster-assembled films remain constant [5,6]. The different grain dimensions determine a different concentration of grain boundaries influencing the electron motion, as can be seen by extracting the electron mean free path values from the fit of ρt vs. t curves.

In order to study the trend of the mean free path as function of grain size, we fabricated two different types of ns-Au/Ar films (Ar1 and Ar2) with grain size of 5 nm and 9 nm respectively and we compared the resulting values with the mean free path in ns-Au\He films. In Figure 10 we report the average mean free path values for gold cluster-assembled films resulting from different size distributions and the value obtained for evaporated films. We observe that the electron mean free paths in cluster-assembled films are systematically smaller than that of atom-assembled Au films and, in particular, it increases as a function of the average cluster size.

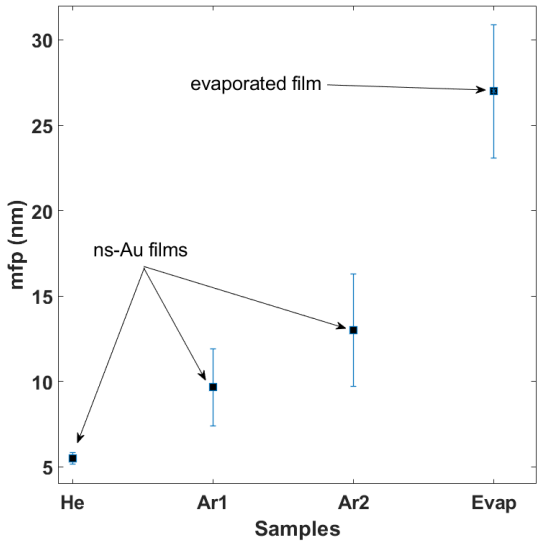

Figure 10. Mean-free path values extracted from the fitting procedure for ns-Au/He films, ns-Au/Ar samples deposited with different mean clusters dimension (Ar1 - 5 nm and Ar2 - 9 nm) and evaporated films. The error bars associated to each class are computed as the standard deviation of mean-free path values of the fabricated samples.

The highly disordered structure of cluster-assembled films due to the extremely large number of grain boundaries [6] increase the electron scattering rate and, as consequence, the interference

between backscattered and flowing electrons, thus modifying the effective conduction electron density.

These phenomena could also explain the higher p parameter observed for the ns-Au/He samples. In these systems, the high density of grain boundaries resulting from their small size significantly modify the film resistance, since the electron, during its motion, meets several boundaries and undergoes several scattering events. Consequently, equation (2) fits well the experimental curves considering extremely small mean free paths. Higher *p* values, that translate in a minor fraction of electrons randomly scattered at the surfaces [2,42], shows that in this case, the surface scattering plays a minor role with respect to the modification of the electron mean free path to describe well the evolution of resistance as function of the thickness.

Although we excluded the grain boundary contribution from the analysis, the description given by equations (1) and (2) allows to account for anomalous values of thin film resistivity with respect to bulk one and different trend of percolation curves of analyzed nanostructured films [2,44,45,46]. Elements like complex interplay between disordered morphology and confinement of electron conduction in nanoscale structures should be considered in a more refined model in order to completely describe the observed electrical behavior.

4 Conclusions

We have characterized the growth process of cluster-assembled gold films from sub-monolayer to a continuous layer beyond the electrical percolation threshold, highlighting the correlation between the nanostructure and the electrical properties. The influence of different cluster size distributions on the onset of the electrical conduction and the role of defects have been investigated by combining in situ and ex situ electrical and structural characterizations.

We observed a significant departure from the electrical behavior reported in the literature for polycrystalline metallic thin films. This originates from the use of different building blocks: atoms in the case of polycrystalline films and clusters in the case of nanogranular films. The assembling of clusters has a profound influence on the structural and functional properties of the systems: the number and the nature of defects in cluster-assembled metallic films are substantially different from those of polycrystalline ones. This aspect suggests that the evolution of the electrical properties with the film growth and, in particular, of the percolation curve is determined not only by geometric parameters but also by the internal structure of the clusters used as building blocks.

Our results provide the evidence of the complex role of nanoscale texture and defects in the electrical properties of metallic films assembled by clusters that retain, at least partially, their individuality; the understanding and control of structural and functional parameters of the building

blocks by varying cluster dimension, crystalline structure and chemical composition can open interesting avenues for the synthesis of systems with controlled non-linear electrical and optical properties [47,48]. In particular, in view of the development of robust and scalable fabrication bottom-up technologies of devices for unconventional computing [13].

References

[1] D. Valencia *et al.*, "Grain-Boundary Resistance in Copper Interconnects: From an Atomistic Model to a Neural Network" *Phys. Rev. Appl.*, **9**, 044005 (2018)

[2] R. C. Munoz and C. Arenas, "Size effects and charge transport in metals : Quantum theory of the resistivity of nanometric metallic structures arising from electron scattering by grain boundaries and by rough surfaces" *Appl. Phys. Rev.*, **4**, 011102 (2017)

[3] D. Gall, "Electron mean free path in elemental metals" *J. Appl. Phys.*, **119**, 085101 (2016)

[4] D. Gall, "The search for the most conductive metal for narrow interconnect lines" *J. Appl. Physic*, **127**, 050901 (2020)

[5] M. Mirigliano and P. Milani, "Electrical conduction in nanogranular cluster-assembled metallic films" *Adv. Phys. X*, **6**, 1908847 (2021)

[6] M. Mirigliano, S. Radice, A. Falqui, A. Casu, F. Cavaliere, and P. Milani, "Anomalous electrical conduction and negative temperature coefficient of resistance in nanostructured gold resistive switching films" *Sci. Rep.*, **10**, 1 (2020)

[7] E. Barborini *et al.*, "The influence of nanoscale morphology on the resistivity of cluster-assembled nanostructured metallic thin films" *New J. Phys.*, **12**, 073001 (2010)

[8] I. A. Gladskikh, M. G. Gushchin, and T. A. Vartanyan, "Resistance Switching in Ag, Au, and Cu Films at the Percolation Threshold" *Semiconductors*, **52**, 671 (2018)

[9] R. Henriquez, S. Bravo, R. Roco, V. Del Campo, D. Kroeger, and P. Häberle, "Electrical Percolation and Aging of Gold Films" *Metall. Mater. Trans. A Phys. Metall. Mater. Sci.*, **50**, 493 (2019)

[10] M. Mirigliano, F. Borghi, A. Podestà, A. Antidormi, L. Colombo, and P. Milani, "Non-ohmic behavior and resistive switching of Au cluster-assembled films beyond the percolation threshold" *Nanoscale Adv.*, **1**, 3119 (2019)

[11] M. Mirigliano *et al.*, "Complex electrical spiking activity in resistive switching nanostructured Au two-terminal devices" *Nanotechnology*, **31**, 234001 (2020)

[12] W. Tarantino and L. Colombo, "Modeling resistive switching in nanogranular metal films" *Phys. Rev. Res.*, **2**, 043389 (2020)

[13] M. Mirigliano *et al.*, "A binary classifier based on a reconfigurable dense network of metallic nanojunctions" *Neuromorph. Comput. Eng.,* **1**, 024007 (2021)

[14] H. Jaeger, "Towards a generalized theory comprising digital, neuromorphic and unconventional computing" *Neuromorphic Comput. Eng.*, **1**, 012002 (2021)

[15] K. Wegner, P. Piseri, H. V. Tafreshi, and P. Milani, "Cluster beam deposition: A tool for nanoscale science and technology" *J. Phys. D. Appl. Phys.*, **39**, R439 (2006)

[16] P. Piseri, H. V. Tafreshi, and P. Milani, "Manipulation of nanoparticles in supersonic beams for the production of nanostructured materials" *Curr. Opin. Solid State Mater. Sci.*, **8**, 195 (2004)

[17] H. V. Tafreshi, P. Piseri, G. Benedek, and P. Milani, "The Role of Gas Dynamics in Operation Conditions of a Pulsed Microplasma Cluster Source for Nanostructured Thin Films Deposition" *J. Nanosci. Nanotechnol.*, **6**, 1140 (2006)

[18] F. Borghi, A. Podestà, C. Piazzoni, and P. Milani, "Growth Mechanism of Cluster-Assembled Surfaces: From Submonolayer to Thin-Film Regime" *Phys. Rev. Appl.*, **9**, 044016 (2018)

[19] F. Borghi, M. Mirigliano, P. Milani, and A. Podestà, "Quantitative Analysis of Gold Nano-aggregates by Combining Electron and Probe Microscopy Techniques" , in *Toward a Science Campus in Milan*, 2018, 67

[20] F. Borghi, M. Milani, L. G. Bettini, A. Podestà, and P. Milani, "Quantitative characterization of the interfacial morphology and bulk porosity of nanoporous cluster-assembled carbon thin films" *Appl. Surf. Sci.*, **479**, 395 (2019)

[21] A. Podestà *et al.*, "Cluster-assembled nanostructured titanium oxide films with tailored

wettability" *J. Phys. Chem. C*, **113**, 18264 (2009)
[22] A. Zangwill, *Physics at Surfaces*, First Edit. Cambridge, 1988
[23] P. Jensen, "Growth of nanostructures by cluster deposition: Experiments and simple models" *Rev. Mod. Phys.*, **71**, 1695 (1999)
[24] B. Yoon *et al.*, "Morphology control of the supported islands grown from soft-landed clusters" *Surf. Sci.*, **443**, 76 (1999)
[25] L. Bardotti *et al.*, "Diffusion and aggregation of large antimony and gold clusters deposited on graphite" *Surf. Sci.*, **367**, 276 (1996)
[26] A. Lassesson, S. A. Brown, J. Van Lith, and M. Schulze, "Electrical characterization of gold island films: A route to control of nanoparticle deposition" *Appl. Phys. Lett.*, **93**, 2 (2008)
[27] S. Yamamuro, K. Sumiyama, T. Hihara, and K. Suzuki, "Geometrical and electrical percolation in nanometre-sized Co-cluster assemblies" *J. Phys. Condens. Matter*, **11**, 3247 (1999)
[28] F. Family and T. Vicsek, "Scaling of the active zone in the Eden process on percolation networks and the ballistic deposition model" *J. Phys. A. Math. Gen.*, **18**, L75 (1985)
[29] A.-L. Barabási and H. E. Stanley, *Fractal Concepts in Surface Growth*. CAMBRIDGE University Press, 1995
[30] K. Banerjee, J. Shamanna, and S. Ray, "Surface morphology of a modified ballistic deposition model" *Phys. Rev. E - Stat. Nonlinear, Soft Matter Phys.*, **90**, 3 (2014)
[31] H. F. El-Nashar, W. Wang, and H. A. Cerdeira, "Surface growth kinetics and morphological structural transition in a (2 + 1)-dimensional deposition model" *J. Phys. Condens. Matter*, **8**, 3271 (1996)
[32] F. Borghi *et al.*, "Cluster-assembled cubic zirconia films with tunable and stable nanoscale morphology against thermal annealing" *J. Appl. Phys.*, **120**, 055302 (2016)
[33] A. Podestà, F. Borghi, M. Indrieri, S. Bovio, C. Piazzoni, and P. Milani, "Nanomanufacturing of titania interfaces with controlled structural and functional properties by supersonic cluster beam deposition" *J. Appl. Phys.*, **118**, 234309 (2015)
[34] F. Marín, G. Gray, C. Gonzalez-Fuentes, V. del Campo, P. Häberle, and R. Henríquez, "Electrical transport during growth, aging and oxidation of copper ultrathin films before percolation" *Results Phys.*, **19**, 0 (2020)
[35] P. Melinon *et al.*, "Comparison of molecular and cluster deposition: Evidence of different percolation processes" *Phys. Rev. B*, **44**, 12562 (1991)
[36] P. Jensen *et al.*, "Direct observation of the infinite percolation cluster in thin films: Evidence for a double percolation porcess" *Phys. Rev. B*, **47**, 5008 (1993)
[37] B. Lutzer, O. Bethge, C. Zimmermann, J. Smoliner, and E. Bertagnolli, "*In situ* resistance measurements during physical vapor deposition of ultrathin metal films on Si(111) at room temperature" *J. Vac. Sci. Technol. B, Nanotechnol. Microelectron. Mater. Process. Meas. Phenom.*, **35**, 051802 (2017)
[38] M. Cattani and M. C. Salvadori, "Contribution of the morphological grain sizes to the electrical resistivity of platinum and gold thin films" *Surf. Rev. Lett.*, **11**, 463 (2004)
[39] H. Scher and R. Zallen, "Critical Density in Percolation Processes" *J. Chem. Phys.*, **53**, 3759 (1970)
[40] J. Vancea, H. Hoffmann, and K. Kastner, "Mean Free Path and Effective Density of Conduction Electrons in Polycrystalline Metal Films" *Thin Solid Films*, **121**, 201 (1984)
[41] Y. Namba, "Resistivity and Temperature Coefficient of Thin Metal Films with Rough Surface" *Jpn. J. Appl. Phys.*, **9**, 1326 (1970)
[42] E. H. Sondheimer, "The mean free path of electrons in metals" *Adv. Phys.*, **1**, 1 (1952)
[43] A. F. Mayadas and M. Shatzkes, "Electrical-resistivity model for polycrystalline films: the case of arbitrary reflection at external surfaces" *Phys. Rev. B*, **1**, 1382 (1970)
[44] L. Moraga, C. Arenas, R. Henriquez, S. Bravo, and B. Solis, "The electrical conductivity of polycrystalline metallic films" *Phys. B Condens. Matter*, **499**, 17 (2016)

[45] G. Reiss, J. Vancea, and H. Hoffmann, “Grain-Boundary Resistance in polycrystalline Metals” *Phys. Rev. Lett.*, **56**, 2100 (1986)
[46] X. Y. Qin, W. Zhang, L. D. Zhang, and L. D. Jiang, “Low-temperature resistance and its temperature dependence in nanostructured silver” *Phys. Rev. B*, **56**, 596 (1997)
[47] S. M. Arakelian, I. Chestenov, A. V Istratov, T. A. Khudaiberganov, and O. Y. Butkovskiy, “Nonlinear Dynamic Modeling for High Temperature Superconductivity in Nanocluster Topological Structures on Solid Surface” , in *New Trends in Nonlinear Dynamics*, W. Lacarbonara, B. Balachandran, J. Ma, J. A. T. Machado, and G. Stepan, Eds. Springer, 2019
[48] S. N. Bagayev, S. M. Arakelian, A. O. Kucherik, D. N. Bukharov, and O. Y. Butkovsky, “Nano-Optics of Thin-Film Laser-Induced Topological Structures on a Solid Surface: Fundamental Phenomena and Their Applications” *Bull. Russ. Acad. Sci. Phys.*, **84**, 1427 (2020)